Multi-band Carrier Phase Positioning toward 6G: Performance Bounds and Design Insights

Ehsan Shourezari*, Mehmet C. Ilter*, Ossi Kaltiokallio*, Jukka Talvitie*, Gonzalo Seco-Granados†, Henk Wymeersch‡, and Mikko Valkama*

*Department of Electrical Engineering, Tampere University, Finland

†Universitat Autonoma de Barcelona, Barcelona, Spain

‡Department of Electrical Engineering, Chalmers University of Technology, Sweden

***Abstract*—Carrier phase positioning (CPP) is widely used in satellite system applications, enabling centimeter-level localization accuracy. Recently, CPP is gaining attraction also in terrestrial mobile networks, particularly in 5G New Radio (NR) evolution toward 6G. One key challenge is to resolve the so-called integer ambiguity problem, as carrier phase provides only relative position information. This work introduces and studies a multi-band CPP scenario with intra- and inter-band carrier aggregation (CA) opportunities across FR1, mmWave-FR2, and emerging 6G FR3 bands. Specifically, we derive multi-band CPP performance bounds, showcasing the superiority of multi-band CPP for high-precision localization in current and future mobile networks. A wide collection of numerical results is provided, covering the impacts of the available carrier bandwidth, number of aggregated carriers, transmit power, and the number of network nodes. The offered results highlight that only two carriers need to be aggregated to substantially facilitate resolving the integer ambiguity problem.**

***Index Terms*—Positioning and sensing, carrier phase positioning, 5G NR and 6G, Cramér-Rao lower bound, carrier aggregation.**

I. Introduction

Carrier phase positioning (CPP) is known to enable precise ranging, facilitating accuracies from sub-meter down to centimeter levels [1]. CPP methods are already well-established in global navigation satellite system (GNSS) context [2], while the use of carrier phase measurements has recently been explored also in the 3rd Generation Partnership Project (3GPP) standardization, particularly in the context of 5G-Advanced, as an emerging technology for enhanced positioning capabilities in mobile terrestrial networks [3], [4].

In general, the core principle of CPP lies in accurately measuring the carrier phase, enabling ranging precision within fractions of a wavelength [1]. A key technical challenge in utilizing carrier phase measurements is the *integer ambiguity problem* [5] which results from the fact that the carrier phase does not reveal the integer number of full wavelengths between the transmitter and the receiver. Furthermore, in most systems, achieving strict time synchronization between nodes is challenging, and clock biases can impede accurate integer ambiguity estimation in single-point positioning [6]. The integer ambiguity problem can be addressed by combining phase and time measurements, performing double-differential phase measurements across multiple base station (BS) pairs, and ensuring phase consistency across signals from different directions [7]. In the context of 5G New Radio (NR) mobile networks, the CPP has been recently studied in [3], [8], [9], with main focus on single-band measurements and signal processing algorithms. Additionally, [10] introduced and derived performance bounds for localizing a user equipment (UE) under a mutual clock bias using time-of-arrival (ToA) and phase measurements, focusing again on the single-band scenario.

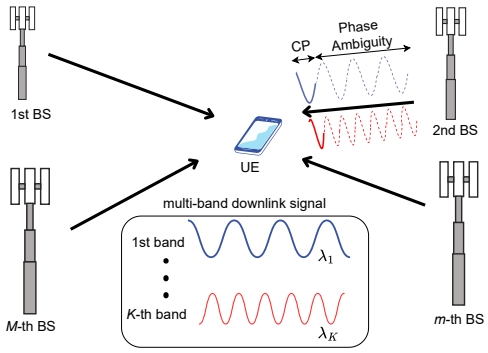

Fig. 1. Multi-band CPP system model with K bands and M network nodes.

In parallel, carrier aggregation (CA) is a key technology in mobile networks, enabling the aggregation of fragmented spectrum resources [11] for increased data rates. The NR CA mechanism applies to FR1 (sub-6 GHz) and FR2 (24.25-71 GHz), supporting various band combinations. Additionally, new spectrum is expected to be allocated for 6G networks within the 7-24 GHz range (FR3), which balances wider bandwidth, lower attenuation, and reduced hardware costs [12]. Importantly, CA can improve also the achievable positioning accuracy as it enlarges the effective bandwidth by combining positioning reference signals (PRSs) from multiple component carriers [13]. To this end, [14] proposed joint estimation of ToA using reference symbols obtained from multiple frequency bands. Similarly, [15] proposed a CA-based integrated sensing and communication mechanism for improved sensing performance.

In this work, inspired by the cellular CA technology and the clear demand for super-resolution positioning, we study and investigate the *multi-band CPP* problem illustrated conceptually in Fig. 1. We cover multi-band phase measurements in both intra-band and inter-band CA scenarios, while consider all the three frequency ranges (FR1, FR2, and FR3) that are of interest in 3GPP. We address the multi-band CPP from the fundamental performance bounds perspective, and the key technical contributions of this work can be stated as follows:

- We formulate a model for the delay and phase observations in a multi-band multiple-BS downlink transmission, explicitly highlighting the integer ambiguity problem;
- We introduce and derive the so-called mixed-integer Cramér-Rao bound (MICRB), specifically tailored for the considered multi-band observation model. This provides the fundamental position error bound (PEB) for multi-band CPP;
- We offer a large collection of numerical results and the corresponding numerical performance bounds, covering the impacts of the carrier bandwidth, number of aggregated carriers, and the number of network nodes or BSs;
- We utilize the derived bounds and the numerical results to provide insight on the multi-band operation impacts on the feasibility of obtaining the integer ambiguities and exploiting carrier phase measurements for positioning. Importantly, the bounds reveal that aggregating only two carriers is already largely relaxing the integer ambiguity problem.

The rest of the paper is organized as follows. Section II presents the CPP system model with the delay and carrier phase measurements. Section III introduces the multi-band observation model and derives the fundamental bounds. Section IV provides numerical results under various scenarios, and validates the tightness of the bounds. Finally, Section V concludes the paper.

II. Multi-band CPP System Model

We consider a scenario with a single UE and $M \geq N_d + 1$ BSs, where $N_d \in \{2, 3\}$ represents the dimension of the position coordinates (i.e., 2D or 3D positions, respectively). The UE has an unknown position $\boldsymbol{x}_{\rm ue} \in \mathbb{R}^{N_d}$ and is subject to clock bias wrt. the BSs. We further assume that the BSs are mutually time- and phase-synchronized and have known locations $\boldsymbol{x}_{{\rm bs},m} \in \mathbb{R}^{N_d}$. Terminology-wise, we note that we use the notion of 'BS', however, the system model is also applicable with distributed transmission/reception points (TRPs) of a single BS – or similarly with TRPs or antenna points of a future cell-free or distributed MIMO (D-MIMO) system. Moreover, for simplicity, we assume that any frequency offsets among all entities have been corrected.

At the k-th band, each BS transmits a unit-modulus OFDM reference signal for M OFDM symbols, e.g. 5G PRS, over N_k subcarriers with spacing $\Delta_{f,k}$ and transmit power $P_{{\rm tx},k}$. The reference signal transmission of the M BSs are orthogonalized, with each BS utilizing different subcarriers per OFDM symbol following the classical comb structure. At the UE side, the frequency-domain received signal from m-th BS and k-th band under the ideal line-of-sight (LoS) condition is given by [16]

$$\boldsymbol{y}_{m,k} = \sqrt{E_{s,k}}\alpha_{m,k}\boldsymbol{d}(\tau_{m,k}) + \boldsymbol{\omega}_{m,k}, \tag{1}$$

such that $\boldsymbol{y}_{m,k} \in \mathbb{C}^{N_k \times 1}$. Herein, $E_{s,k} = P_{{\rm tx},k}/(N_k\Delta_{f,k})$ is the energy per subcarrier, $\alpha_{m,k} = \rho_{m,k}e^{-j\vartheta_{m,k}}$ represents the complex channel gain in which $\rho_{m,k}$ captures the effect of path loss and transmitter and receiver antenna gains, $\vartheta_{m,k}$ is the carrier phase, $\tau_{m,k}$ is the ToA, and $\boldsymbol{d}(\tau_{m,k})$ is the channel response of the m-th BS for the k-th band with $[\boldsymbol{d}(\tau_{m,k})]_n = e^{-j2\pi n\Delta_{f,k}\tau_{m,k}}$ for $n \in \{0, \cdots, N_k - 1\} - (N_k - 1)/2$, and $k \in \{1, \ldots, K\}$. The additive white Gaussian noise (AWGN) $\boldsymbol{\omega}_{m,k} \in \mathbb{C}^{N_k \times 1}$ has the statistics $\boldsymbol{\omega}_{m,k} \sim \mathcal{N}(\boldsymbol{0}, \sigma_\omega^2\boldsymbol{I})$, where σ_ω^2 is the noise power spectral density. The noise vectors for different bands or BSs are assumed to be independent.

Due to the mutually-synchronized BSs, the ToA and carrier phase measurements across multiple frequency bands and BSs characterize the geometric relationship between the UE and the BSs as follows [17]

$$\tau_{m,k} = \frac{1}{c}\ell_m + B_{\rm ue} \tag{2}$$

$$\vartheta_{m,k} = \frac{2\pi}{\lambda_k}\ell_m + 2\pi f_{c,k}B_{\rm ue} + \phi_{{\rm ue},k} \tag{3}$$

where $\ell_m = \|\boldsymbol{x}_{{\rm bs},m} - \boldsymbol{x}_{\rm ue}\|$ is the actual distance between the BS and UE, $B_{\rm ue}$ is the clock bias of the UE relative to the network/BSs clock that is propagated to both the time and carrier phase measurements, and $\phi_{\rm ue,k}$ is the phase offset of the UE that is assumed to be band-dependent. Furthermore, $f_{c,k} = c/\lambda_k$ is the carrier frequency of the k-th band, with λ_k denoting the corresponding wavelength, and c is the speed-of-light.

The considered CPP mechanism follows a two-stage process. First, the ToA and carrier phase are estimated from $\boldsymbol{y}_{m,k}$, as $\hat{\tau}_{m,k}$ and $\hat{\vartheta}_{m,k}$. Then, these estimates are used to determine the UE position. Note that $\hat{\vartheta}_{m,k}$ is an estimate of $\frac{2\pi}{\lambda_k}\ell_m + 2\pi f_{c,k}B_{\rm ue} + \phi_{{\rm ue},k}$ modulo 2π. Hence, we can express the ToA and phase observations as distances $y_{\tau,m,k} = \hat{\tau}_{m,k} \times c$ and $y_{\vartheta,m,k} = \hat{\vartheta}_{m,k} \times \frac{\lambda_k}{2\pi}$, given by

$$y_{\tau,m,k} = \ell_m + B_{\rm ue}c + \omega_{\tau,m,k} \tag{4}$$

$$y_{\vartheta,m,k} = \ell_m + B_{\rm ue}c + z_{m,k}\lambda_k + \phi_{{\rm ue},k}\frac{\lambda_k}{2\pi} + \omega_{\vartheta,m,k}. \tag{5}$$

Herein, $z_{m,k} \in \mathbb{Z}$ is the unknown integer ambiguity, with the actual value given by $z_{m,k} = -\left\lfloor \left(\frac{\lambda_k}{2\pi}\vartheta_{m,k} + \omega_{\vartheta,m,k}\right)/\lambda_k \right\rfloor$, where "$\lfloor\,\rfloor$" returns the greatest integer less than or equal to its input. The terms $\omega_{\tau,m,k}$ and $\omega_{\vartheta,m,k}$ represent zero-mean Gaussian noise affecting the ToA and phase measurements, respectively. Both terms are expressed in the distance domain, and are independent of each other. By deriving the Fisher information matrix (FIM) for the observation model (1) wrt. $\tau_{m,k}$ and $\vartheta_{m,k}$, it can be shown that the lower bounds for the covariances of $\omega_{\tau,m,k}$ and $\omega_{\vartheta,m,k}$ read $\sigma^2_{\tau,m,k} \simeq 3c^2/(2\,\gamma_{m,k}\pi^2W_k^2)$ and $\sigma^2_{\vartheta,m,k} = \lambda_k^2/(8\,\gamma_{m,k}\pi^2)$, respectively [10]. Herein, $\gamma_{m,k} = N_kE_{s,k}\rho^2_{m,k}/\sigma^2_\omega$ is the signal to noise energy ratio, called SNR from now on, where $W_k = N_k\Delta_{f,k}$ is the available passband width at band k.

By gathering the observations from different BSs and frequency bands, we define $\boldsymbol{y} = \left[\boldsymbol{y}_\tau^\top, \boldsymbol{y}_\vartheta^\top\right]^\top$ where both $\boldsymbol{y}_\tau$ and $\boldsymbol{y}_\vartheta$ are structured as $\boldsymbol{y}_\star = [y_{\star,1,1}, y_{\star,2,1}, \ldots, y_{\star,M,K}]^\top \in \mathbb{R}^{KM\times 1}$. The superscript "$\top$" stands for transpose. Similarly, we build the effective noise vectors $\boldsymbol{\omega}_\tau$, $\boldsymbol{\omega}_\vartheta$ by gathering $\omega_{\tau,m,k}$ and $\omega_{\vartheta,m,k}$, respectively. Their corresponding diagonal covariance matrices, $\boldsymbol{\Sigma}_\tau$ and $\boldsymbol{\Sigma}_\vartheta$, are defined as $\boldsymbol{\Sigma}_\star = {\rm diag}([\sigma^2_{\star,1,1}, \sigma^2_{\star,2,1}, \ldots, \sigma^2_{\star,M,K}]^\top)$, where "diag" generates a diagonal matrix from its vector input. We further introduce $\boldsymbol{\eta} = \left[\boldsymbol{s}^\top, \boldsymbol{z}^\top\right]^\top \in \mathbb{R}^{(K+N_d+1)\times 1} \times \mathbb{Z}^{KM\times 1}$ as the unknown parameter vector, where $\boldsymbol{z} = [z_{1,1}, z_{2,1}, \ldots, z_{M,K}]^\top$, while $\boldsymbol{s} = \left[\boldsymbol{x}_{\rm ue}^\top, B_{\rm ue}, \boldsymbol{\phi}_{\rm ue}^\top\right]^\top$ and $\boldsymbol{\phi}_{\rm ue} = [\phi_{{\rm ue},1}, \ldots, \phi_{{\rm ue},K}]^\top$.

III. Multi-Band CPP Performance Bounds

A. Multi-band Observation Model

To initiate the MICRB derivation, we first organize the stacked delay and phase observations building on (4)-(5) as

$$\boldsymbol{y} = \tilde{\boldsymbol{f}}(\tilde{\boldsymbol{s}}) + \boldsymbol{B}\boldsymbol{z} + \boldsymbol{B}\boldsymbol{\varphi} + \boldsymbol{\omega}, \tag{6}$$

where $\tilde{\boldsymbol{s}} = \left[\boldsymbol{x}_{\rm ue}^\top, B_{\rm ue}\right]^\top$, $\boldsymbol{\varphi} = \frac{1}{2\pi}\boldsymbol{\phi}_{\rm ue} \otimes \mathbf{1}_{M\times 1} \in \mathbb{R}^{KM\times 1}$, and "$\otimes$" shows the Kronecker product. The matrix $\boldsymbol{B}$ is defined as $\boldsymbol{B} = \left[\mathbf{0}_{KM\times KM} \;\; \boldsymbol{\Lambda}\right]^\top$ with $\boldsymbol{\Lambda} = \mathrm{diag}([\lambda_1, \cdots, \lambda_K]^\top) \otimes \boldsymbol{I}_M \in \mathbb{R}^{KM\times KM}$. The noise is stacked as $\boldsymbol{\omega} = \left[\boldsymbol{\omega}_\tau^\top, \boldsymbol{\omega}_\vartheta^\top\right]^\top$ with $\boldsymbol{\omega} \sim \mathcal{N}(\mathbf{0}_{2KM\times 1}, \boldsymbol{\Sigma}_{\rm ch})$, and $\boldsymbol{\Sigma}_{\rm ch} = \mathrm{blkdiag}(\boldsymbol{\Sigma}_\tau, \boldsymbol{\Sigma}_\vartheta)$. Here, "blkdiag" builds a block-diagonal matrix, while $\mathbf{0}$, $\mathbf{1}$, and $\boldsymbol{I}$ denote all-0, all-1, and identity matrices, respectively. The vector function $\tilde{\boldsymbol{f}}(\tilde{\boldsymbol{s}})$ is defined for its j-th entry as

$$[\tilde{\boldsymbol{f}}(\tilde{\boldsymbol{s}})]_j = \|\boldsymbol{x}_{{\rm bs},\mathrm{mod}(j-1,M)+1} - \boldsymbol{x}_{\rm ue}\| + B_{\rm ue}c. \tag{7}$$

We note that $\boldsymbol{\varphi}$ and $\boldsymbol{z}$ are not jointly identifiable, making the system under-determined, but since both $\boldsymbol{z}$ and $\boldsymbol{\phi}_{\rm ue}$ are eventually nuisance parameters, the state dimension can be reduced by incorporating $\phi_{{\rm ue},k}$ into one of the integer ambiguities of the k-th band. Without loss of generality, by merging each $\phi_{{\rm ue},k}$ with $z_{1,k}$, the reduced state variables for the k-th band become $\phi_{{\rm d},k} = \frac{\phi_{{\rm ue},k}}{2\pi} + z_{1,k}$ and $[z_{2,k} - z_{1,k}, \ldots, z_{M,k} - z_{1,k}]^\top \in \mathbb{Z}^{(M-1)\times 1}$. Accordingly, (6) can be reformulated using the combined parameters as

$$\boldsymbol{y} = \tilde{\boldsymbol{f}}(\tilde{\boldsymbol{s}}) + \boldsymbol{B}\boldsymbol{E}\boldsymbol{z}_{\rm d} + \boldsymbol{B}\boldsymbol{\varphi}_{\rm d} + \boldsymbol{\omega}, \tag{8}$$

where $\boldsymbol{z}_{\rm d} = \boldsymbol{D}\boldsymbol{z} \in \mathbb{Z}^{K(M-1)\times 1}$ denotes the multi-band differential (reduced-dimension) integer ambiguity vector, and the combined phase offset is $\boldsymbol{\varphi}_{\rm d} = \boldsymbol{\phi}_{\rm d} \otimes \mathbf{1}_{M\times 1} \in \mathbb{R}^{KM\times 1}$ with $\boldsymbol{\phi}_{\rm d} = [\phi_{{\rm d},1}, \cdots, \phi_{{\rm d},K}]^\top$. Both $\boldsymbol{D}$ and $\boldsymbol{E}$ are block-diagonal matrices, with each block corresponding to a band. Matrix $\boldsymbol{D} = \boldsymbol{I}_K \otimes \left[-\mathbf{1}_{(M-1)\times 1} \; \boldsymbol{I}_{(M-1)}\right] \in \mathbb{R}^{K(M-1)\times KM}$ acts as a differentiator, reducing the dimension of the integer vector in each band. On the other hand, matrix $\boldsymbol{E} = \boldsymbol{I}_K \otimes \left[\mathbf{0}_{(M-1)\times 1} \; \boldsymbol{I}_{(M-1)}\right]^\top \in \mathbb{R}^{KM\times K(M-1)}$ inserts a zero as the first row of each reduced-dimension integer block. Now, we can collect all the real-valued unknowns into $\boldsymbol{f}(\boldsymbol{s}) = \tilde{\boldsymbol{f}}(\tilde{\boldsymbol{s}}) + \boldsymbol{B}\boldsymbol{\varphi}_{\rm d}$ and rewrite (8) as

$$\boldsymbol{y} = \boldsymbol{f}(\boldsymbol{s}) + \boldsymbol{B}\boldsymbol{E}\boldsymbol{z}_{\rm d} + \boldsymbol{\omega}. \tag{9}$$

This observation model serves as the basis of the MICRB derivation, in which with a slight change of variables, $\boldsymbol{s}$ is redefined as $\boldsymbol{s} = \left[\boldsymbol{x}_{\rm ue}^\top, B_{\rm ue}, \boldsymbol{\phi}_{\rm d}^\top\right]^\top \in \mathbb{R}^{(K+N_d+1)\times 1}$.

B. Multi-Band Known-Integer and Mixed-Integer CRBs

For conventional estimation problems with ordinary real- or complex-valued parameters, such as ToA-based positioning, the Cramér-Rao bound (CRB) on the error covariance is obtained from the inverse of the FIM [18]. However, in the CPP problem at hand, the conventional FIM approach *cannot be applied* since the derivatives in FIM calculation cannot be computed with respect to *integer-valued* parameters. Instead, we derive and compute the so-called multi-band mixed-integer CRB as follows: We first assume that the relaxed integer ambiguities, considered as ordinary real numbers, are given with the error covariance equal to the CRB of the relaxed observation model. Next, to incorporate the integer nature of the parameters into the bound derivation, we find the integer least squares (ILS) estimation of the ambiguities. This transforms the remaining part of the problem into the *real-valued* domain, referred to as the *known-integer* problem. However, any error in the estimated integer ambiguities from the ILS stage introduces a bias in $\boldsymbol{s}$. Thus, in the final stage, we compute the MICRB as the lower bound for the error covariance of a biased estimator of $\boldsymbol{s}$, based on the theoretical framework presented in [19].

As stated, we start by assuming that the real-valued relaxed ambiguity variables are given, with an error covariance equal to the corresponding CRB. Before proceeding, we ensure that all parameters are identifiable in the relaxed observation model. Using (8) as the baseline, the observation model with the relaxed identifiable parameters takes the form

$$\boldsymbol{y} = \tilde{\boldsymbol{f}}(\tilde{\boldsymbol{s}}) + \boldsymbol{B}\boldsymbol{z}_{\rm rlx} + \boldsymbol{\omega}, \tag{10}$$

from which, by computing the CRB of $\boldsymbol{z}_{\rm rlx}$, denoted by $\boldsymbol{\Sigma}_{\rm rlx}$, we can build the given real-valued ambiguities as follow

$$\hat{\boldsymbol{z}}_{\rm rlx} = \boldsymbol{E}\boldsymbol{z}_{\rm d} + \boldsymbol{\varphi}_{\rm d} + \boldsymbol{u}, \;\; \boldsymbol{u} \sim \mathcal{N}(\mathbf{0}_{KM\times 1}, \boldsymbol{\Sigma}_{\rm rlx}). \tag{11}$$

The detailed expression of $\boldsymbol{\Sigma}_{\rm rlx}$ is provided in Appendix A. Next, to eliminate $\boldsymbol{\varphi}_{\rm d}$ from $\boldsymbol{z}_{\rm rlx}$, we multiply both sides of (11) by $\boldsymbol{D}$, yielding the differential observations of the form

$$\boldsymbol{r} = \boldsymbol{D}\boldsymbol{E}\boldsymbol{z}_{\rm d} + \boldsymbol{D}\boldsymbol{\varphi}_{\rm d} + \boldsymbol{D}\boldsymbol{u} = \boldsymbol{z}_{\rm d} + \boldsymbol{D}\boldsymbol{u}, \tag{12}$$

which follow from the equalities $\boldsymbol{D}\boldsymbol{E} = \boldsymbol{I}$ and $\boldsymbol{D}\boldsymbol{\varphi}_{\rm d} = \mathbf{0}$ (to prove, consider the multiplications block by block). Finally, we recover $\boldsymbol{z}_{\rm d}$ by solving the ILS problem, written as

$$\hat{\boldsymbol{z}}_{\rm d} = \underset{\boldsymbol{z}_{\rm d}\in\mathbb{Z}^{K(M-1)\times 1}}{\arg\min} \; (\boldsymbol{r} - \boldsymbol{z}_{\rm d})^\top \boldsymbol{S}^{-1} (\boldsymbol{r} - \boldsymbol{z}_{\rm d}), \;\; \boldsymbol{S} = \boldsymbol{D}\boldsymbol{\Sigma}_{\rm rlx}\boldsymbol{D}. \tag{13}$$

In general, any error in $\boldsymbol{z}_{\rm d}$ leads to a bias in $\boldsymbol{s}$. To determine this bias, we linearize (9) around $\boldsymbol{s}$, which yields $\boldsymbol{y} = \boldsymbol{f}(\boldsymbol{s}) + \boldsymbol{A}_{\boldsymbol{f}}\boldsymbol{\delta s} + \boldsymbol{B}\boldsymbol{E}\boldsymbol{z}_{\rm d} + \boldsymbol{\omega}$, where $\boldsymbol{A}_{\boldsymbol{f}} = \nabla_{\boldsymbol{s}}\boldsymbol{f}(\boldsymbol{s}) \in \mathbb{R}^{2KM\times(K+N_d+1)}$ is computed at the true value of $\boldsymbol{s}$. In the absence of any error in $\boldsymbol{z}_{\rm d}$, i.e., when $\hat{\boldsymbol{z}}_{\rm d} = \boldsymbol{z}_{\rm d}$, the WLS estimate of $\boldsymbol{\delta s}$ is given by

$$\widehat{\boldsymbol{\delta s}} = \left(\boldsymbol{\Sigma}_{\rm ch}^{-1/2}\boldsymbol{A}_{\boldsymbol{f}}\right)^\dagger \boldsymbol{\Sigma}_{\rm ch}^{-1/2} \left(\boldsymbol{y} - \boldsymbol{f}(\boldsymbol{s}) - \boldsymbol{B}\boldsymbol{E}\hat{\boldsymbol{z}}_{\rm d}\right), \tag{14}$$

which is an unbiased zero-mean estimator. However, if there is an integer error $\boldsymbol{\delta}_z$ in the solution to the integer program (13), such that $\hat{\boldsymbol{z}}_{\rm d} = \boldsymbol{z}_{\rm d} + \boldsymbol{\delta}_z$, the resulting estimate $\widehat{\boldsymbol{\delta s}}$ will be biased. This bias, which also reflects the bias in $\boldsymbol{s}$, is derived from the structure of (14) and is given by

$$\boldsymbol{b}(\boldsymbol{s}|\boldsymbol{\delta}_z) = -\left(\boldsymbol{\Sigma}_{\rm ch}^{-1/2}\boldsymbol{A}_{\boldsymbol{f}}\right)^\dagger \boldsymbol{\Sigma}_{\rm ch}^{-1/2}\boldsymbol{B}\boldsymbol{E}\boldsymbol{\delta}_z \tag{15}$$

Now, the observation model is turned into a known integer one, i.e., no integer unknown remains. In order to compute the MICRB, we first note that when the estimators of $\boldsymbol{s}$ are biased with bias $\boldsymbol{b}(\boldsymbol{s}|\boldsymbol{\delta}_z)$, the corresponding lower bound of the error covariance, accounting for this bias, is given by [19]

$$\boldsymbol{\Sigma}_{\rm mi}(\boldsymbol{s}|\boldsymbol{\delta}_z) = \boldsymbol{b}(\boldsymbol{s}|\boldsymbol{\delta}_z)\boldsymbol{b}(\boldsymbol{s}|\boldsymbol{\delta}_z)^\top + (\boldsymbol{I} + \boldsymbol{A}_{\boldsymbol{b}})\boldsymbol{\Sigma}_{\rm known}(\boldsymbol{I} + \boldsymbol{A}_{\boldsymbol{b}})^\top \tag{16}$$

where $\boldsymbol{A}_{\boldsymbol{b}} = \nabla_{\boldsymbol{s}}\boldsymbol{b}(\boldsymbol{s}|\boldsymbol{\delta}_z) \in \mathbb{R}^{(K+N_d+1)\times(K+N_d+1)}$. In the usual case that the bias is not very sensitive to $\boldsymbol{s}$, $\boldsymbol{A}_b \approx \mathbf{0}$, and $\boldsymbol{\Sigma}_{\rm known}$ represents the *ultimate* lower bound on the error covariance for the measurement model in which the reduced-state integer ambiguities, $\boldsymbol{z}_{\rm d}$, are known. The detail formulation of $\boldsymbol{J}_{\rm known} = \boldsymbol{\Sigma}_{\rm known}^{-1}$ can be found in Appendix B. The corresponding bound is called *known-integer* bound in the following.

Finally, the proposed MICRB can be obtained by taking the expectation with respect to the integer ambiguity error as

$$\boldsymbol{\Sigma}_{\text{mi}}(\boldsymbol{s}) = \mathbb{E}_{\boldsymbol{\delta}_z}\left[\boldsymbol{\Sigma}_{\text{mi}}(\boldsymbol{s}|\boldsymbol{\delta}_z)\right] \approx \frac{1}{N_{\text{mc}}}\sum_{i=1}^{N_{\text{mc}}} \boldsymbol{\Sigma}_{\text{mi}}(\boldsymbol{s}|\boldsymbol{\delta}_z^{(i)}) \quad (17)$$

where N_{mc} is number of Monte-Carlo simulations. As represented in (17), the expectation can be numerically computed using Monte-Carlo simulations. Since (13) is invariant wrt. $\boldsymbol{z}_{\text{d}}$, the Monte-Carlo approach simplifies to generating N_{mc} samples of a Gaussian noise, $\boldsymbol{r}^{(i)} \sim \mathcal{N}(\boldsymbol{0}, \boldsymbol{S})$, and directly determining the estimate $\boldsymbol{\delta}_z^{(i)} = \hat{\boldsymbol{z}}_{\text{d}}^{(i)}$ using (13). Hence, the floating solution of the original problem is actually not needed to obtain the MICRB. Finally, $\boldsymbol{\Sigma}_{\text{mi}}(\boldsymbol{x}_{\text{ue}}) = [\boldsymbol{\Sigma}_{\text{mi}}(\boldsymbol{s})]_{1:N_d,1:N_d}$. Overall, computing the MICRB requires only the geometry matrix $\boldsymbol{A_b}$, along with $\boldsymbol{\Sigma}_{\text{rlx}}$, $\boldsymbol{\Sigma}_{\text{ch}}$, and $\boldsymbol{\Sigma}_{\text{known}}$.

C. Multi-band Delay-Only Reference Bound

As an important benchmark, besides the known-integer bound, we consider the bound for the observation model that exploits only the ToA measurements and thus drops $\boldsymbol{y}_\vartheta$. In this case, the unknown parameters will be $\tilde{\boldsymbol{s}} = \left[\boldsymbol{x}_{\text{ue}}^\top, B_{\text{ue}}\right]^\top$, and the corresponding FIM can be formulated as

$$\boldsymbol{J}_{\text{delay}} = \begin{bmatrix} \tilde{\boldsymbol{U}}\boldsymbol{J}_\tau\tilde{\boldsymbol{U}}^\top & c\tilde{\boldsymbol{U}}\,\text{diag}(\boldsymbol{J}_\tau) \\ c(\tilde{\boldsymbol{U}}\,\text{diag}(\boldsymbol{J}_\tau))^\top & \text{tr}(\boldsymbol{J}_\tau)c^2 \end{bmatrix}, \quad (18)$$

where $\boldsymbol{J}_\tau = \boldsymbol{\Sigma}_\tau^{-1}$, "tr" is the trace operation, and $\tilde{\boldsymbol{U}} = \boldsymbol{1}_{1\times K} \otimes \boldsymbol{U} \in \mathbb{R}^{N_d \times KM}$ denotes the transposed Jacobian of $[\tilde{\boldsymbol{f}}(\tilde{\boldsymbol{s}})]_{1:KM}$ wrt. $\boldsymbol{x}_{\text{ue}}$, with $\boldsymbol{U} = [\boldsymbol{u}_1, \boldsymbol{u}_2, \ldots, \boldsymbol{u}_M]$, and $\boldsymbol{u}_{\text{m}} = (\boldsymbol{x}_{\text{ue}} - \boldsymbol{x}_{\text{bs},m})/\ell_m$. Then, we obtain $\boldsymbol{\Sigma}_{\text{delay}}(\boldsymbol{x}_{\text{ue}}) = \left[\boldsymbol{J}_{\text{delay}}^{-1}\right]_{1:N_d,1:N_d}$. This lower bound is greater in value than the known-integer bound since it disregards the phase measurements. Thus, the difference between the delay-only bound and the derived known-integer and mixed-integer bounds tells the potential performance gains available through the phase measurements.

IV. Numerical Results and Insights

We next investigate and evaluate the derived multi-band CPP bounds in a concrete network deployment context. We consider an example physical scenario where the UE is fixed at the location $\boldsymbol{x}_{\text{ue}} = [0\,0]^\top$, while M BSs are randomly located in the surrounding 2D space with $\boldsymbol{x}_{\text{bs},m} \sim \mathcal{N}(\boldsymbol{0}, (0.1\,\text{km})^2\boldsymbol{I}_{2\times 2})$. The following default system parameters are utilized, unless otherwise stated: subcarrier spacing $\Delta_{f,k} = 30\,\text{kHz}$, $N_k = 612$ active subcarriers, noise power spectral density of $-174\,\text{dBm/Hz}$, a receiver noise figure of 13 dB, and $M = 6$ BSs. We model the magnitude of the channel gain as $\rho_{m,k} = \lambda_{\text{ref}}/(4\pi\ell_m)$ with $\lambda_{\text{ref}} = 3\,\text{cm}$. Therefore, we assume that transceiver array gain essentially compensates the dependence of the path loss factor on the center-frequency. The default per-band transmit power is $P_{\text{tx},k} = 0\,\text{dBm}$. As the default carrier frequencies at different bands, we use $f_c = 3.5\,\text{GHz}$ (FR1), $f_c = 28\,\text{GHz}$ (FR2), and $f_c = 12\,\text{GHz}$ (FR3), unless otherwise stated.

To assess and compare parameter impacts, we use the metric $\text{PEB} = \sqrt{\text{tr}(\boldsymbol{\Sigma}_\star(\boldsymbol{x}_{\text{ue}}))}$ for all the mixed-integer, known-integer, and delay-only cases. The proposed MICRB given in (17) is computed over $N_{\text{mc}} = 1\,000$ Monte-Carlo samples.

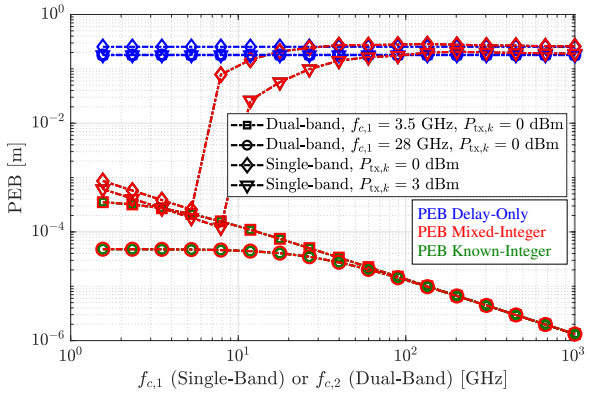

Fig. 2. Impact of the carrier frequency on the different PEBs. For the single-band case, a doubled P_{tx} case is also shown for comparison and fairness.

A. Carrier Frequency and Multi-band Measurements

We start by illustrating the impact of carrier frequency while also comparing the single-band and dual-band scenarios. The results are shown in Fig. 2. In the single-band case, $f_{c,1}$ varies, whereas in the dual-band case $f_{c,1}$ is fixed and $f_{c,2}$ varies. The delay-only PEB ($\text{PEB}_{\text{delay}}$) appears unaffected by the carrier frequency, as it primarily depends on SNR and bandwidth rather than the frequency (assuming a constant SNR across bands). In contrast, the known-integer PEB ($\text{PEB}_{\text{known}}$) – plotted only for the dual-band case for readability of the figure – improves with increasing carrier frequency since shorter wavelengths reduce the power of the measurement noise in (5). In mathematical terms, $\text{PEB}_{\text{known}}$ is governed by $\boldsymbol{\Sigma}_\vartheta$, which improves as λ decreases. For the higher values of $f_{c,2}$, the influence of $f_{c,1}$ disappears, and both dual-band cases coincide.

Furthermore, the behavior of the proposed mixed-integer PEBs (PEB_{mi}) reveals additional insights. In the single-band case, the PEB_{mi} curves converge to $\text{PEB}_{\text{known}}$ for carrier frequencies below $f_{c,1} = 9\,\text{GHz}$ (duplicated power) and $f_{c,1} = 5\,\text{GHz}$ (default power). This means that the reduced-state ambiguities are fully resolved in these frequency ranges. At higher frequencies, however, the curves diverge since shorter wavelengths lower the probability of correct ambiguity resolution. In other words, the integer problem in (13) becomes harder to solve correctly at higher frequencies. In the dual-band case, unlike single-band scenario, no divergence is observed, and PEB_{mi} coincides with $\text{PEB}_{\text{known}}$ across all $f_{c,2}$ values. This robustness stems from the increased number of informative observations, which enables more reliable ambiguity resolution. Even when $f_{c,1} = 28\,\text{GHz}$ and $f_{c,2} > 100\,\text{GHz}$, we still have $\text{PEB}_{\text{mi}} = \text{PEB}_{\text{known}}$.

Next, Fig. 3 illustrates the combined effect of carrier frequency and the number of measurement bands, K. To fairly assess the impact of the number of bands, we maintain constant sum-power of $K \times P_{\text{tx},k} = 0\,\text{dBm}$ for any given K. For $K = 1$, all curves correspond to $f_{c,1} = 3.5\,\text{GHz}$, while when K increases from 2 to 10, we include sequentially the following carrier frequencies in the different bands: FR1: $[3.6\!:\!0.2\!:\!5.2]$ GHz, FR2: $[24\!:\!1\!:\!32]$ GHz, and FR3: $[8\!:\!0.5\!:\!12]$ GHz. Thus overall, FR1 adopts intra-band CA, while the other cases correspond to inter-band CA. Now, as can be observed in Fig. 3, the $\text{PEB}_{\text{delay}}$ remains constant because the increased number of

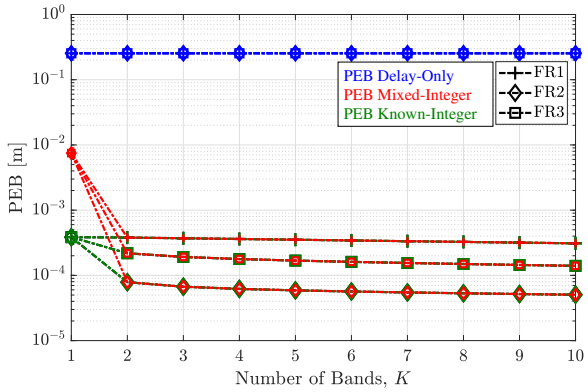

Fig. 3. PEB vs. the number of measurement frequencies, K. In all cases, the first carrier frequency ($f_{c,1}$) correspond to 3.5 GHz, while the additional frequencies follow the frequency ranges indicated in the text.

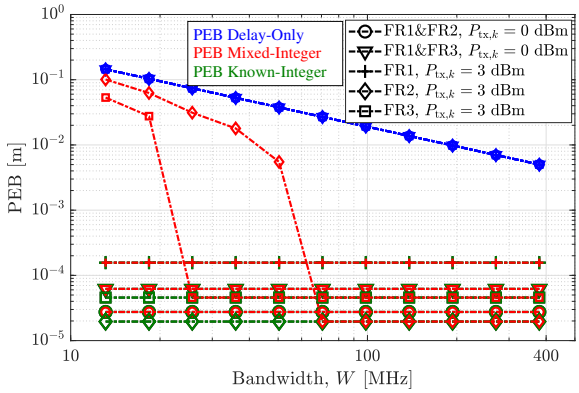

Fig. 4. Impact of the carrier bandwidth, W, on the PEBs.

measurements is offset by the reduced transmit power per band, as K increases. In contrast, $\text{PEB}_{\text{known}}$ and $\text{PEB}_{\text{known}}$ improve for two reasons. First, having more bands introduces additional measurements that contain new information about the location, as the integer ambiguities differ across bands. This effect is especially noticeable when increasing from a single-band to dual-band. Second, the higher carrier frequencies of the added bands tighten the bound, as previously discussed in Fig. 2. For $K \geq 2$, PEB_{mi} is completely coincided with $\text{PEB}_{\text{known}}$.

B. Carrier Bandwidth

We next examine the effect of increasing the carrier bandwidth by increasing the number of subcarriers. As shown in Fig. 4, the improvement in time resolution due to the increased bandwidth improves $\text{PEB}_{\text{delay}}$ across all cases. However, $\text{PEB}_{\text{known}}$ remains nearly constant, as phase estimation accuracy is largely independent of the bandwidth. In single-band FR2 and FR3, smaller bandwidths lead to higher mixed-integer PEB due to two factors: the high delay measurement errors and severe integer ambiguity errors caused by the shorter wavelengths in these frequency ranges. By comparison, in the single-band FR1, the smaller integer ambiguities and easier integer resolution compensate for the higher delay-only error covariance, allowing PEB_{mi} to fully converge to $\text{PEB}_{\text{known}}$. On the other hand, in dual-band scenarios, PEB_{mi} curves completely coincide with $\text{PEB}_{\text{known}}$ curves and are tighter than single-band FR1, due to the increased number of independent observations and aggregation with higher frequencies.

From Figs. 2 and 4, three key insights emerge: (*i*) Higher frequencies are advantageous when the setup allows for perfectly resolving the integer ambiguities; (*ii*) Lower frequencies are more effective when the signal characteristics, such as low bandwidth, prevent perfect ambiguity resolution at high frequencies; (*iii*) The multi-band mechanism balances these two behaviors and improves ambiguity resolution over a broader range of the involved parameters.

C. Power Budget

Next, we examine the impact of transmit power on the PEB performance. Additionally, we account for the practical aspect of greater bandwidth availability at higher carrier frequencies,

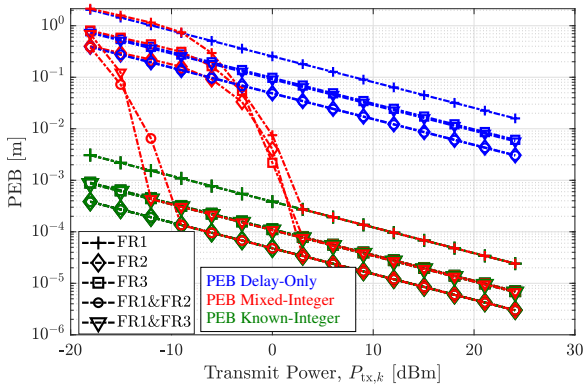

Fig. 5. Impact of TX power on the PEBs while also considering different carrier bandwidths at different bands. In FR1, FR2, and FR3, there are 51×12, 264×12, and 133×12 subcarriers with 30 kHz spacing, respectively.

with details as shown along the caption of Fig. 5. To this end, as observed in Fig. 5, increasing the transmit power enhances the SNR, which in turn improves both $\text{PEB}_{\text{delay}}$ and $\text{PEB}_{\text{known}}$ linearly. The behavior of the different PEB_{mi} curves aligns with the earlier observations in Fig. 2. This plot further reinforces the motivation for utilizing multi-band measurements, as a given PEB level can be reached with substantially smaller transmit power – the difference being in the order of 10 dB. Such is a major benefit from the power consumption perspective.

D. Comparison to Single-band Bounds and Their Fusion

We next compare the single-band bounds proposed in [10], their fusion across bands, and the proposed multi-band bounds in our work. To obtain the fusion of separate single-band cases, we sum up the FIMs of each band and compute the corresponding covariance matrices. Since each band has distinct phase offsets, we focus on the effective part of each FIM (the inverse of the upper-left $(N_d + 1) \times (N_d + 1)$ block of the corresponding covariance matrix), which corresponds to the user coordinates and clock bias parameters shared across all bands[1].

As shown in Fig. 6, the $\text{PEB}_{\text{known}}$ and $\text{PEB}_{\text{delay}}$ bounds are identical in both the multi-band and the band-fusion cases, since different bands provide linear measurements with independent noise and real-valued phase offsets which are solved independently for each band. Therefore, the multi-band

[1]The effective part of the FIM matrix is obtained by computing the Schur complement of the FIM block associated with the phase offset.

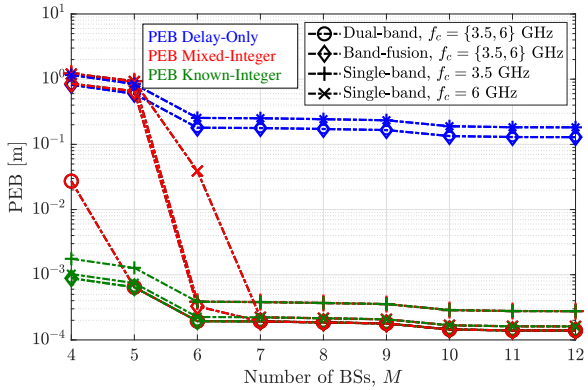

Fig. 6. Comparison between the multi-band and single-band fusion approaches while also varying the number of base-stations, M.

FIM is equal to the sum of the individual FIMs. However, for PEB_{mi}, since the integer ambiguities are interrelated across the bands, the proposed multi-band bound combines the information coherently, enabling better ambiguity resolution and yielding a tighter bound than the band-fusion case. The effect of the number of BSs, M, is also assessed and highlighted. While increasing M generally improves performance, the improvement is not strictly linear due to the randomness in BS placement. Importantly, the multi-band mixed-integer PEB reaches convergence with fewer BSs than the other cases.

V. Conclusion

This work addressed multi-band carrier phase positioning, integrating both intra-band and inter-band carrier aggregation to enhance positioning accuracy. We introduced and derived the so-called mixed-integer CRB (MICRB), specifically designed for multi-band carrier phase positioning. As critical performance benchmarks, we also derived the lower bounds for delay-only and known integer ambiguity cases. The analysis highlights the advantages of multi-band positioning measurements, demonstrating their ability to improve localization accuracy over single-band approaches – particularly in resolving integer ambiguities and thereby reducing positioning errors. Additionally, we showed the impacts of different carrier frequencies, bandwidths and number of BSs, offering valuable design insights for next-generation positioning systems. Notably, it was shown that aggregating only two carriers already yields significant gains in resolving the ambiguity problem. Our future research will cover sensitivity analysis to practical aspects such as multipath propagation and network side clock imperfections. Additionally, efficient estimation algorithms reaching the derived bounds will be pursued.

Appendix A
Multi-Band Relaxed Integer Ambiguity Bound

We consider $\boldsymbol{z}_{\text{rlx}}$ as a real-valued parameter vector in (10). Accordingly, the unknown parameter vector is defined as $\boldsymbol{\eta} = [\tilde{\boldsymbol{s}}^\top, \boldsymbol{z}_{\text{rlx}}{}^\top]^\top \in \mathbb{R}^{(KM+N_d+1)\times 1}$, By applying the Schur complement to the corresponding FIM, it can be shown that the lower bound for the error covariance of $\boldsymbol{z}_{\text{rlx}} \in \mathbb{R}^{KM\times 1}$ is then of the form

$$\boldsymbol{\Sigma}_{\text{rlx}} = \boldsymbol{\Lambda}^{-1}\Big(\boldsymbol{\Sigma}_{\vartheta} + \begin{bmatrix}\tilde{\boldsymbol{U}}^\top c\mathbf{1}_{KM\times 1}\end{bmatrix} \boldsymbol{J}_{\text{delay}}^{-1} \begin{bmatrix}\tilde{\boldsymbol{U}} \\ c\mathbf{1}_{1\times KM}\end{bmatrix}\Big)\boldsymbol{\Lambda}^{-1}. \quad (19)$$

Note that $\boldsymbol{\Lambda}$, $\tilde{\boldsymbol{U}}$, and $\boldsymbol{J}_{\text{delay}}$ are already defined in (6), (18). Furthermore, for observation model (10), it can be shown that the CRB of $\tilde{\boldsymbol{s}}$ is the same as the delay-only case in (18).

Appendix B
Multi-Band Known Integer Ambiguity Bound

When $\boldsymbol{z}_{\text{d}}$ is known in (8), the FIM of $\boldsymbol{s}$ is given by

$$\boldsymbol{J}_{\text{known}} = \begin{bmatrix} \tilde{\boldsymbol{U}}\boldsymbol{J}\tilde{\boldsymbol{U}}^\top & c\tilde{\boldsymbol{U}}\text{diag}(\boldsymbol{J}) & \tilde{\boldsymbol{U}}\boldsymbol{J}_{\vartheta}\hat{\boldsymbol{\Lambda}}^\top \\ c(\tilde{\boldsymbol{U}}\text{diag}(\boldsymbol{J}))^\top & \text{tr}(\boldsymbol{J})c^2 & c(\tilde{\boldsymbol{\Lambda}}\text{diag}(\boldsymbol{J}_{\vartheta}))^\top \\ \tilde{\boldsymbol{\Lambda}}(\tilde{\boldsymbol{U}}\boldsymbol{J}_{\vartheta})^\top & c\tilde{\boldsymbol{\Lambda}}\text{diag}(\boldsymbol{J}_{\vartheta}) & \tilde{\boldsymbol{\Lambda}}\boldsymbol{J}_{\vartheta}\tilde{\boldsymbol{\Lambda}}^\top \end{bmatrix}, \quad (20)$$

where $\boldsymbol{J} = \boldsymbol{J}_{\vartheta} + \boldsymbol{J}_{\tau}$, and $\boldsymbol{J}_{\star} = \boldsymbol{\Sigma}_{\star}^{-1}$, $\tilde{\boldsymbol{\Lambda}} = \text{diag}([\lambda_1, \ldots, \lambda_K]^\top) \otimes \mathbf{1}_{1\times M} \in \mathbb{R}^{K\times KM}$. Taking the inverse of $\boldsymbol{J}_{\text{known}}$, the CRB on the position reads as $\boldsymbol{\Sigma}_{\text{known}}(\boldsymbol{x}_{\text{ue}}) = [\boldsymbol{J}_{\text{known}}]^{-1}_{1:N_d,1:N_d}$.

References

[1] J. Nikonowicz, A. Mahmood, M. I. Ashraf, E. Björnson, and M. Gidlund, "Indoor Positioning in 5G-Advanced: Challenges and Solution Toward Centimeter-Level Accuracy with Carrier Phase Enhancements," *IEEE Wireless Commun.*, vol. 31, no. 4, 2024.

[2] W. Ding, W. Sun, Y. Gao, and J. Wu, "Carrier phase-based precise heading and pitch estimation using a low-cost GNSS receiver," *Remote Sensing*, vol. 13, no. 18, p. 3642, 2021.

[3] 3GPP, "Study on Expanded and Improved NR Positioning (Release 18)," Tech. Rep. TR 38.859, June 2024.

[4] N. González-Prelcic *et al.*, "The integrated sensing and communication revolution for 6G: Vision, techniques, and applications," *Proceedings of the IEEE*, vol. 112, no. 7, pp. 676–723, 2024.

[5] J. Talvitie, M. Säily, and M. Valkama, "Orientation and Location Tracking of XR Devices: 5G Carrier Phase-Based Methods," *IEEE J. Sel. Topics Signal Process.*, vol. 17, no. 5, pp. 919–934, 2023.

[6] X. Zhang, T. Wang, Z. Yao, and M. Lu, "Centimeter-level carrier phase positioning for ground-based positioning system without synchronization," *IEEE Trans. Veh. Technol.*, vol. 73, no. 10, pp. 15 345–15 358, 2024.

[7] K. Berntorp, A. Weiss, and S. D. Cairano, "Integer ambiguity resolution by mixture Kalman filter for improved GNSS precision," *IEEE Trans. Aerosp. Electron. Syst.*, vol. 56, no. 4, pp. 3170–3181, 2020.

[8] L. Chen, X. Zhou, F. Chen, L.-L. Yang, and R. Chen, "Carrier phase ranging for indoor positioning with 5G NR signals," *IEEE Internet of Things J.*, vol. 9, no. 13, 2022.

[9] S. Fan, W. Ni, H. Tian, Z. Huang, and R. Zeng, "Carrier phase-based synchronization and high-accuracy positioning in 5G new radio cellular networks," *IEEE Trans. Commun.*, vol. 70, no. 1, pp. 564–577, 2022.

[10] H. Wymeersch, R. Amiri, and G. Seco-Granados, "Fundamental Performance Bounds for Carrier Phase Positioning in Cellular Networks," in *Proc. IEEE GLOBECOM*, 2023, pp. 7478–7483.

[11] X. Han *et al.*, "Flexible spectrum orchestration of carrier aggregation for 5G-advanced," *IEEE Commun. Stand. Mag.*, vol. 7, no. 4, 2023.

[12] Z. Cui, P. Zhang, and S. Pollin, "6G wireless communications in 7-24 GHz band: Opportunities, techniques, and challenges," *arXiv preprint arXiv:2310.06425*, 2023.

[13] M. Säily *et al.*, "Positioning technology trends and solutions toward 6G," in *Proc. IEEE PIMRC*, 2021, pp. 1–7.

[14] W. Xu, S. Shojaee, and K. Manolakis, "Carrier-aggregated timing estimation for radio positioning," in *Proc. IEEE VTC-Spring*, 2019.

[15] Z. Wei *et al.*, "Carrier aggregation enabled integrated sensing and communication signal design and processing," *IEEE Trans. Veh. Technol.*, vol. 73, no. 3, pp. 3580–3596, 2024.

[16] H. Wymeersch and G. Seco-Granados, "Radio localization and sensing—Part I: Fundamentals," *IEEE Communications Letters*, vol. 26, no. 12, pp. 2816–2820, 2022.

[17] J. S. Subirana, J. M. J. Zornoza, and M. Hernández-Pajares, *ESA TM-23 GNSS Data Processing*. European Space Agency, 2013.

[18] S. M. Kay, *Fundamentals of Statistical Signal Processing: Estimation Theory*. Prentice-Hall, Inc., 1993.

[19] Y. Eldar, "Uniformly Improving the Cramér-Rao Bound and Maximum-Likelihood Estimation," *IEEE Trans. Signal Process.*, vol. 54, no. 8, pp. 2943–2956, 2006.